Petroleum Science 23 (2026) 3556–3575

Contents lists available at ScienceDirect

Petroleum Science

journal homepage: www.keaipublishing.com/en/journals/petroleum-science

Original Paper

In-situ combustion of heavy oil within a vuggy carbonate reservoir: Part II—Mechanism of permeability inversion and rock fabric transformation

Rita Fazlyeva [a], Tagir Karamov [b,*], Matthew Ursenbach [a], Roberto Aguilera [a], Andrey Voropaev [c], Mikhail Spasennykh [b], Gordon Moore [a], Alexey Cheremisin [b], Mehta Sudarshan [a]

[a] Chemical and Petroleum Engineering Department, University of Calgary, 2500 University Drive NW, Calgary, Alberta T2N 1N4, Canada
[b] Center for Petroleum Science and Engineering, Skolkovo Institute of Science and Technology, Moscow, 121205, Russia
[c] Hydroisotop GmbH, Woelkestrasse 9, Schweitenkirchen, 85301, Germany

ARTICLE INFO

Article history:
Received 9 September 2025
Received in revised form
26 January 2026
Accepted 5 February 2026
Available online 11 February 2026

Edited by Yan-Hua Sun

Keywords:
In-situ combustion
Carbonates
Dolomite reservoir
Isotope
XRD
EDX

ABSTRACT

Predicting the performance of in-situ combustion (ISC) in carbonate reservoirs is notoriously challenging. This study reveals a paradoxical permeability inversion phenomenon: initially high-permeability grainstones (up to 2600 mD) suffer catastrophic permeability damage, while initially low-permeability packstones (below 250 mD) show marked improvement. We demonstrate that this counter-intuitive behavior is driven by the thermal decomposition of dolomite. This process fundamentally transforms the rock fabric, shifting it from a robust, grain-supported architecture (grainstone/packstone) to a fragile, matrix-supported texture (wackstone-like), which critically reduces pore throat radii in high-quality rocks. At the micro-scale, the key agent of this transformation is identified as the neoformation of needle-shaped magnesium-calcium hydrosilicate crystals, which occlude pores and can occupy up to 50% of the pore volume. Stable isotope analysis confirms that this mineralogical alteration is the dominant process, revealing up to 70% of CO_2 produced originates from dolomite decomposition rather than hydrocarbon combustion. These findings prove that initial reservoir quality is a poor predictor of ISC performance; instead, the geochemical reactivity and thermal stability of the rock fabric are paramount. We therefore propose the rock-fabric number as a more robust metric for predicting reservoir response to thermal EOR processes.

© 2026 The Authors. Publishing services by Elsevier B.V. on behalf of KeAi Communications Co. Ltd. This is an open access article under the CC BY license (http://creativecommons.org/licenses/by/4.0/).

1. Introduction

More than 50% of heavy oil (Akbar et al., 2000) is contained in carbonates, which are some of the most prolific and challenging reservoirs for oil recovery due to their heterogeneity caused by the complex porous media containing matrix, fractures, vugs, and karsts (Mazzullo, 2004). Air injection has immense potential for hydrocarbon recovery from various reservoirs. Depending on the oil type, it can be implemented either air only, wet combustion or in combination with other steam-based methods.

Despite multiple successful projects recovering oil from the carbonate reservoirs with the application of air-based injection methods (Miller, 1995; Turta et al., 2007), there are certain concerns related to the carbonate precipitation and fines migration that might cause permeability reduction (Hascakir and Kovscek, 2014). Recent experimental studies have confirmed that significant permeability damage can occur during thermal treatment of carbonates (Fazlyeva et al., 2023; Mogensen and Masalmeh, 2020; Tao et al., 2024), though the underlying pore-scale mechanisms are not fully understood. Conversely, thermal breakthrough from the production wells due to the existing fractures remains another major operational challenge (Fatemi, 2009).

While most of the post-burn studies in the in-situ combustion (ISC) literature are focused on the clastic reservoirs (Bennion et al., 1977; Buxton and Pollock, 1974; Hogue et al., 2015; Jha and

* Corresponding author.
E-mail address: T.Karamov@skoltech.ru (T. Karamov).
Peer review under the responsibility of China University of Petroleum (Beijing).

https://doi.org/10.1016/j.petsci.2026.02.008
1995-8226/© 2026 The Authors. Publishing services by Elsevier B.V. on behalf of KeAi Communications Co. Ltd. This is an open access article under the CC BY license (http://creativecommons.org/licenses/by/4.0/).

reservoir rock. Based on this analysis, Sample H was selected for all subsequent experiments due to its high dolomite content (over 70%), which is representative of the target reservoir type. Sample A in Fig. 1, for reference, represents the mineralogical composition of an actual core from the target field, containing 71.2% dolomite, 28.6% calcite, and 0.2% quartz. The selected Sample H is the closest analogue to this benchmark.

To evaluate the pore space structure of the core plugs and the remaining residual inclusions, a GE Phoenix V|tome|x L240 micro-computer tomography scanner was used with a resolution of 30 μ/voxel. To determine the parameters of the pore space, the obtained 3D images were segmented using the GeoDict software of MathToMarket, and parallelepiped voxels of 11003–13003 were used for the calculations. The volume of the analyzed structures is 11–46 mm^3.

Scanning electron microscopy (SEM) was employed for detailed microstructural investigation of rock samples both before and after the combustion tube (CT) experiment. The analyses were conducted using a Thermo Fisher Scientific Quattro S SEM, which accommodates small rock samples (~5 mm in size) chipped off from cores. The electron beam current ranged from 1 pA to 200 nA, with an accelerating voltage between 200 V and 30 kV. The highest spatial resolution achieved was 5 nm. Both secondary electron (SE) and backscattered electron (BSE) imaging modes were utilized during scanning at an accelerating voltage of 10–15 kV (Erdman and Drenzek, 2013). The resulting images had a resolution of 1.536 1.094 pixels.

For semiquantitative elemental composition analysis, an integrated energy-dispersive X-ray spectrometer (EDX; Quantax, Bruker, USA) was used. Lithotyping, structural analysis, and void space characterization were conducted on thin sections using an AxioScope 5 petrographic microscope (ZEISS, Germany), following the Dunham classification system (Dunham and Ham, 1962).

The isotopic composition of carbon, hydrogen, nitrogen, and sulphur in rocks, gases, oils, and water was analyzed using GC-IRMS and EA-IRMS systems. GC-IRMS enabled compound-specific isotope analysis through chromatographic separation, followed by oxidation or pyrolysis at high temperatures (960 or 1400 C) and mass spectrometry. EA-IRMS facilitated bulk isotope measurements by combusting or pyrolyzing samples encapsulated in tin or silver foil at 1020 or 1400 C, with the resulting gases (CO_2, N_2, SO_2, H_2) separated chromatographically before isotopic analysis. Calibration was performed using international standards, including NBS 22 for carbon and hydrogen and IAEA N_2 for nitrogen, with results recalculated relative to international reference scales such as PDB, SMOW, AIR, and CDT. Carbonate carbon isotopes were measured after acid treatment of rock samples with phosphoric acid, while organic carbon isotopes were analyzed post-acid washing. Isotopic measurement precision was 0.2 for carbon, 0.5 for nitrogen and sulphur, and 1.5 for hydrogen. For EA-IRMS analysis, sample aliquots of 0.2–1.0 mg for oil and 0.5–5.0 mg for bulk rock were used. For carbonate-specific analysis, rock powder samples of approximately 0.3 g were reacted with phosphoric acid. A total of 5 rock samples, 5 gas samples, and 7 oil samples were analyzed as part of this study. To ensure analytical reproducibility, each sample was analyzed multiple times (in triplicate), and the average values are reported in the results.

To evaluate reservoir properties of the post-combusted dolomites, a series of helium permeability and porosity measurements were conducted using an AP-608 automated permeameter/porosimeter manufactured by Coretest Sytems. Due to its core holder size limitation, neither the permeability nor porosity of the core plugs used for the CT experiments was possible to measure. Thus, every core plug was represented with a cylindrical miniature core plug length and diameter which were 37.7 and 51 mm, respectively. The miniatures were collected from the same bed of the outcrop and were assumed to have similar properties as their larger analogs.

2.1. Triple-porosity model concept

To mimic real reservoir conditions with severe heterogeneity, a triple-porosity model was chosen: porosity of matrix, fracture, and vug. A detailed description of the experimental setup and procedure was described in the first part of this study (Fazlyeva et al., 2023).

Two types of fractures can be distinguished in this current study. The first one is the crushed dolomite surrounding the core plugs as it has significantly higher permeability values in comparison with the consolidated matrices of the core plugs. Another type of fracture is characterized by the gap between the two parts of the customized core plug: the vug part, and the cap of the core plug itself. Finally, the third type of porosity is presented by the artificially created vug as well as naturally formed vugs during carbonate dissolution.

2.2. Analyses of crushed cores and core plugs: residual saturations

Following the combustion tube experiment, the apparatus was carefully disassembled to analyze the post-burn material. The packed core, which consisted of the dolomite material selected during the initial screening process (analogous to Sample H in Fig. 1), was extracted in sequential segments along the length of the tube, from the production end to the injection end. This segmentation allowed for a detailed analysis of the residual saturations and coke deposition as a function of the distance and maximum temperature reached.

The samples listed in Table 1 (e.g., Core 1-1, Core 2-1, etc.) represent these consecutive segments of crushed dolomite extracted from the combustion tube. Each segment was subjected to a loss on ignition (LOI) test to quantify the amount of coke. During the LOI test, all the core samples placed in the crucibles were heated at 600 C for 16 h. After cooling the samples, they were placed in a desiccator and later weighed. Any mass loss greater than the one observed in the blank test was assumed to be coke. Table 1 shows that some of the samples exceeded 20%, which has been often observed in dolomite samples.

Due to the nature of the packed core, it is impossible to distinctively separate the crushed core from the frac sand as some of the carbonate grains were mixed with and transported to the frac sand and vice-versa. Thus, in reporting the mass loss of the crushed core, the frac sand is also added to the balance, however, it was considered as a non-reactive material and all the losses were related to carbonates only.

Core plugs 1 and 3 were dry-cut in half using a diamond saw. Half of each plug was kept for further visual observation and the other half was crushed and extracted similar to the crushed core pack post-test material to measure the post-test hydrocarbon and water saturation. The coke amount was identified through the LOI test.

Table 2 demonstrates the mass changes of core plugs, maximum temperatures, and saturations before and after the experiment. The average mass loss from the crushed consolidated core material was approximately 4%.

While conducting the CT test and examining the results, it was observed that a substantial quantity of CO_2 was generated in the gaseous phase, surpassing the amount that was anticipated from the combustion reactions of oxygen and oil. The quantity of CO_2 created from the combustion reactions was computed using

Table 1
LOI tests on crushed core samples (from the production end to injection end).

Sample name	Crucible mass, g	Mass of crucible ‡ sample, g		Sample mass, g	LOI, %
		Before	After		
Blank	64.6210	124.5168	119.4508	59.8958	8.46
16 frac sand	63.4564	123.3399	122.6411	59.8835	1.17
20/30 frac sand	62.2476	122.0971	121.9341	59.8495	0.27
20/30 frac sand	69.3262	128.2306	126.5892	58.9044	2.79
Core 1-1	57.1401	118.0624	108.6879	60.9223	15.39
Core 1-2	66.8172	126.6578	118.6239	59.8406	13.43
Core 2-1	71.7523	131.8173	120.1839	60.0650	19.37
Core 2-2	69.4334	129.2020	116.1797	59.7686	21.79
Core 2-3A	67.9130	127.4017	116.2703	59.4887	18.71
Core 2-3B	63.4533	122.9364	105.7232	59.4831	28.94
Core 3-1A	61.9821	121.8645	109.2957	59.8824	20.99
Core 3-1B	73.6066	132.1709	119.6480	58.5643	21.38
Core 3-2	66.6400	126.4443	118.5486	59.8043	13.20
Core 4	55.6236	115.9485	107.6544	60.3249	13.75
Core 5	71.3952	131.6271	122.2258	60.2319	15.61
Core 6	63.1638	113.4620	106.4199	50.2982	14.00
Core 7-1	64.6746	124.6748	117.3123	60.0002	12.27
Core 7-2	60.1279	120.0448	111.8314	59.9169	13.71
Core 8-1	62.6733	122.4833	111.2909	59.8100	18.71
Core 8-2	73.2911	133.6563	121.7397	60.3652	19.74
Core 8-3	57.8073	117.8986	107.4899	60.0913	17.32
Core 8-4	64.4889	124.5150	114.2713	60.0261	17.07
Core 9	70.8309	130.3181	119.3057	59.4872	18.51
Core 10	71.3937	131.5081	119.5802	60.1144	19.84
Core 11-1	63.4527	123.1846	113.2463	59.7319	16.64
Core 11-2	63.4286	123.3451	113.6582	59.9165	16.17
Core 12	70.7956	131.1670	120.6816	60.3714	17.37
Core 13	63.3140	123.5181	113.2725	60.2041	17.02
Core 14-1	60.9472	120.7860	110.6420	59.8388	16.95
Core 14-2	62.2478	122.7955	115.1539	60.5477	12.62
Core 14-3	66.5525	126.0953	116.4433	59.5428	16.21
Core 15	66.5520	126.2972	117.4064	59.7452	14.88
Core 16	68.5229	128.5950	119.5175	60.0721	15.11
Core 17	69.6403	129.5294	120.8246	59.8891	14.53
Frac sand (16 and 20/30)	62.6749	122.7242	121.5525	60.0493	1.95

Table 2
Analysis of core plugs.

	Core plug 1	Core plug 2	Core plug 3	Core plug 4
Vug contained oil?	No	Yes	No	Yes
Between thermocouples	3–4	5–6	7–8	8–9
Initial mass of a core plug (unsaturated), g	428.02	425.30	432.24	446.71
Mass of oil to saturate a core plug, g	24.74	27.47	26.19	19.40
Mass of oil in an artificial vug, g	0.00	7.38	0.00	7.53
Packed mass, g	452.76	460.15	458.43	473.64
Unpacked (post-test) mass, g	408.68	413.38	418.07	431.96
Maximum temperature measured (above/below), C	594/658	632/629	615/577	577/617
Post-test saturation (oil, water, coke), %	0.00/0.13/0.00	ND	0.01/0.07/0.00	ND
Post-test saturation (oil, water, coke), g	0.02/0.53/0.00	ND	0.03/0.29/0.00	ND
Final core mass, g	408.13	ND	413.06	ND
Mass loss, g	19.89	12.24	14.17[a]	14.75[a]
Mass loss, %	4.65	2.88	3.28[a]	3.30[a]
Post-test saturations (oil, water, coke) immediately upstream core plug set, %	0.14/0.00/0.00	0.23/0.00/0.00	0.29/0.01/0.00	0.07/0.00/0.00
Post-test saturations (oil, water, coke) immediately downstream core plug set, %	0.07/0.00/0.00	0.00/0.03/0.00	0.01/0.02/0.74	0.02/0.00/0.00

[a] Not corrected for post-test saturations.

established gas phase parameters, and the difference was associated with the dolomite core decomposition. It was estimated that a total of 963 g of CO_2 was generated due to the decomposition reactions.

To validate the estimated quantity of CO_2 produced from the dolomite decomposition, a comparison was made between the mass of the core that was packed in the CT and the mass of the core retrieved from the post-test sample (with the water and hydrocarbon content subtracted). The difference between the two was found to be 1011 g of core. This value is consistent with 963 g of additional CO_2 produced, as measured in the gas stream. Additionally, this value is well within the margin of uncertainty in all the measurements and computations, thereby indicating that the dolomite decomposition was indeed responsible for the extra CO_2 production. Table 3 provides an overview of the core-CO_2 balance calculations.

Table 3
CO_2 analysis of the crushed core samples and core plugs.

Core sample	Mass before packing, g	Post-test mass, g	Difference, g	Percent decrease in mass, %
Crushed core plus frac sand	20279.1	19329.3	949.8	4.68
Core plugs	1732.3	1671.2[a]	61.1	3.52
Total	22011.3	21000.5	1010.8	4.59
CO_2 associated with decomposition of dolomite core materials[b]				
CO_2, L (ST))			517.4	
CO_2, g			963.2	

[a] This core plug mass accounts for the extraction of Core plugs 1 and 3, but not Core plugs 2 and 4, so this mass includes any water or hydrocarbon still associated with Core pugs 2 and 4. So the total post-test mass may be slightly lower, thereby increasing the difference slightly.
[b] The amount of CO_2 that should have been produced by the combustion reactions was calculated based on values typical of heavy oil combustion reactions. Any CO_2 over that amount was considered to be a product of the decomposition of dolomitic core materials.

3. Results and discussion

3.1. Macroscopic descriptive analysis of the post-burn samples

The post-test core samples were removed in incremental sections and photographed. Fig. 2 presents the unpacked post-burn samples with the maximum temperature values in each zone.

Some vital observations were made during the unpacking process. Generally, the compositional change can be seen from the colors varying from the originally light gray color of the crushed core (Fig. 2(d)). The photographs also show some of the zones less affected by combustion. Despite the termination of air injection after Zone 10, the next zone demonstrated successful oil displacement. Production ended between Zones 11 and 12, where the reservoir saturated with oil as well as the formation of a coke-like wall was observed (Fig. 2(e)). Most of the unrecovered oil was related to this area of the CT.

From the initial visual analysis of the crushed core samples excavated from the tube, two distinguishable colors were observed, and the identified core samples were taken for XRD analysis to identify mineral compositional changes (Fig. 3). Based on the XRD results, the light gray color from the sample taken near Core plug 2 shown in Fig. 2(b) indicates a mineral transition to calcite, while the darker gray contained dominantly dolomite material (sampled from the zone shown in Fig. 2(e)). Besides the thermal decomposition of dolomite and the formation of calcite, fluorapatite was indicated in both samples.

During the macroscopic analysis of the core plugs newly deposited matter on the surface of the vugs were detected. In the case of the core plug samples initially filled with oil, asphaltene/

Fig. 2. Core samples including embedded core plugs with the maximum temperature log.

Fig. 5. Microscopic and macroscopic (center) images of Core plug 2 with the vug (oil-filled).

Fig. 6. Microscopic and macroscopic (center) images of Core plug 4 with the vug (oil-filled).

time scale when compared to the combustion propagation. Thus, Fig. 6 demonstrates that an air-based recovery technique has the potential to involve the oil trapped in the vugs in the production not only through the fracture conductivity but also through the matrix.

3.2. Micro-computed tomography (CT)

As the original core plugs used for the CT study were too large for some of the experiments described further, 1-inch by 1.5-inch miniature core plugs collected from the same part of the layer of

Fig. 8. Micro-CT analysis. (**a**) Plane *Y–Z;* (**b**) plane *X–Z;* (**c**) plane *X–Y;* (**d**) photography of Core plug 4 containing oil.

Differential pore distributions based on the sizes of the examined areas of the samples studied are presented in Fig. 11. It should be noted that the data acquisition size of the miniature and core plugs samples was 20 and 30 μm/voxel, respectively.

It is obvious that the pore distribution of different diameters (big or small) of the core plugs plotted with their miniatures follow similar trends and the deviation is insignificant. This emphasizes the competence of the core plugs vs their miniatures comparison.

3.3. Scanning electron microscopy (SEM)

Fig. 12 shows the initial state of the rock, which is characterized by crystalline dolostones with grain sizes ranging from 0.1 to 0.2 mm. The porosity is predominantly intercrystalline, with pore sizes between 0.01 and 0.1 mm, along with larger vugs measuring from 0.3 to 1.0 mm, evenly distributed throughout the rock. The edges of the dolomite crystals remain intact (indicated by arrows), and no minerals other than dolomite are observed (Fig. 13).

The microstructure and mineralogical composition of the samples after the experiment were analyzed using scanning electron microscopy (SEM) equipped with EDX, thin sections, and XRD techniques. The results of XRD analysis revealed that the samples remained predominantly composed of dolomite (approximately 97%–98%), with minor amounts of anhydrite (2%–3%) observed in samples 17 and 19.

The examination of thin sections indicated the widespread formation of thin organic matter layers on the rock surfaces and the partial filling of individual vugs with organic matter (Fig. 14), which might be residual coke after the experiment.

SEM analysis revealed significant alteration in the newly formed minerals and the grain structure of the rock (Fig. 15). The crystal surfaces became noticeably rough, with the formation of anhydrite as inclusions and as aggregates filling pore spaces (Fig. 15(a, b), the destruction of the initially smooth edge of dolomite (Fig. 15(c)), the rough surface of crystals resulting from the almost complete transformation of dolomite crystals (Fig. 15(d)), and numerous needle-shaped crystals (Fig. 15(e–g)). These crystals were newly formed and such minerals were not observed in the initial samples. The needle-shaped crystals measured up to 20 μm in length and approximately 0.5 μm in thickness, filling up pore space. These newly formed crystals were found exclusively in void spaces, often occupying 20%–30% of the pore volume, with some cases reaching up to 50%. Their exclusive presence in pore spaces suggests that their formation is closely

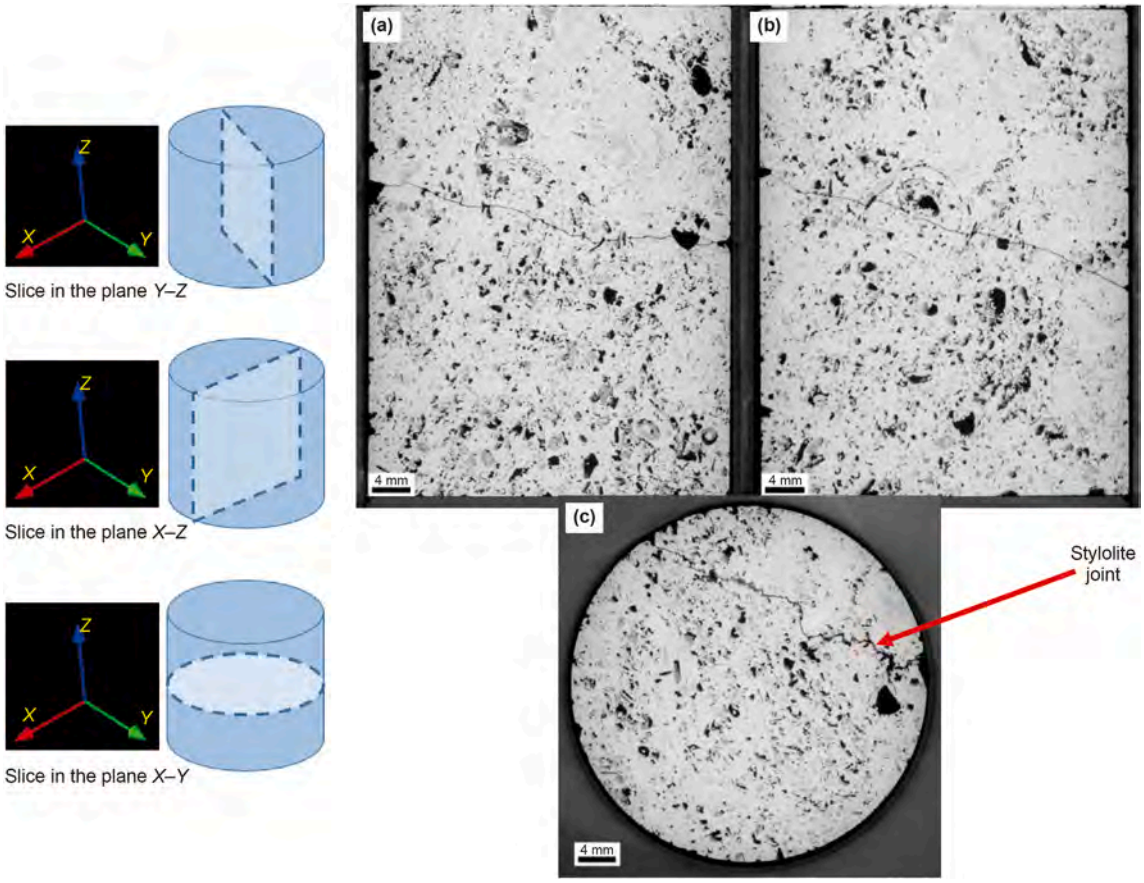

Fig. 9. Micro-CT analysis. (**a**) Plane *Y–Z;* (**b**) plane *X–Z;* (**c**) plane *X–Y* of the miniature Core plug 4.

Table 4
Total porosity results.

Sample	Total porosity, %
Core plug 2	14.19
Core plug 4	11.51
Miniature 2	10.75
Miniature 4	12.68

linked to fluid-related processes, such as changes in fluid composition, temperature, pH, and filtration-related transport within the void spaces.

EDX analysis confirmed anhydrite formation and indicated that the needle-shaped crystals primarily consist of calcium, oxygen, and silicon, with occasional traces of magnesium (Table 5). For instance, in Fig. 14, at point 5, the detected crystals were predominantly composed of Ca, Mg, Si, and O. The overall chemical

Fig. 10. Bulk pore distribution of the porous media (in red). Core plugs 2 (**a**) and 4 (**b**) (30 μm/voxel); miniatures 2 (**c**) and 4 (**d**) (20 μm/voxel).

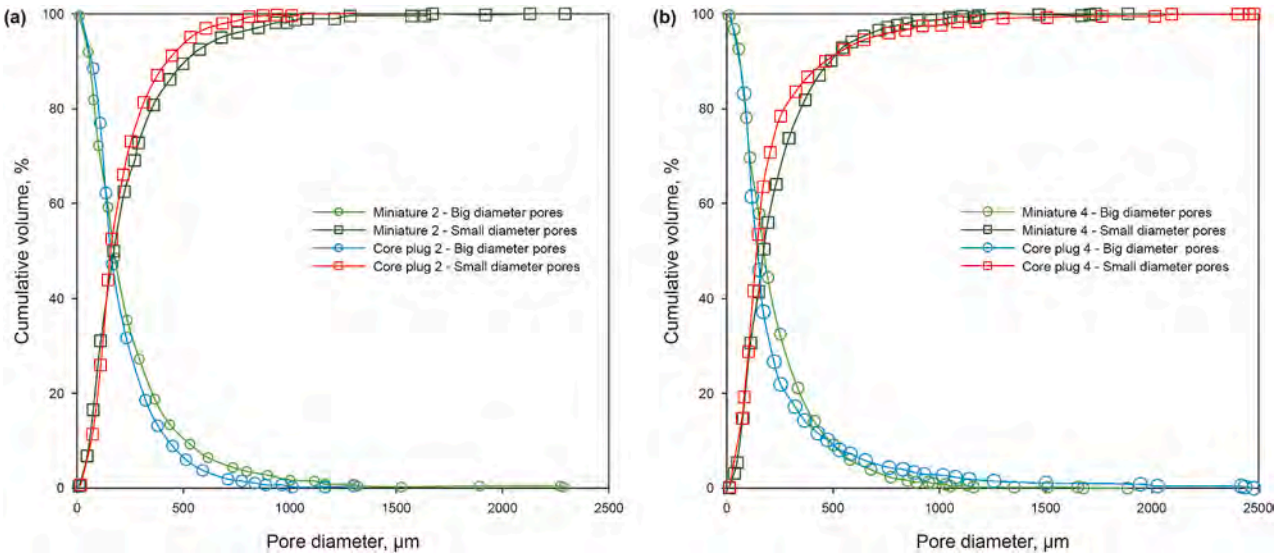

Fig. 11. Pore distribution of Core plugs 2 (**a**) and 4 (**b**) and their miniatures.

Fig. 12. Thin section images of crystalline dolostone samples. Samples 20 (**a**–**c**) and 18 (**c**–**f**) at different magnifications. Pore space includes cavities (C) and intercrystalline pores (P).

composition of the newly formed minerals closely matches that of dolomite (Ca, Mg, C, O), except for the absence of carbon. Carbon was likely removed from the system, potentially as a new compound, such as CO_2.

The microstructure and mineralogy of carbonate rocks subjected to thermal exposure have been previously studied by Karamov et al. (2022). In their work, the decomposition of dolomite resulted in the formation of oxides as complex micro- and nanostructures, along with traces of dolomite destruction.

The formation of anhydrite during thermal treatment was reported by Mukhametdinova et al. (2024) and Subbotina et al. (2023), and attributed to dolomite decomposition through intermediate stages involving $CaCO_3$ and CaO. Sulphur in this case was suggested to originate from fluids such as water or oil. Similarly, Mukhametdinova et al. (2023) described anhydrite formation, though in their study sulphur was derived from pyrite. In all cases, the primary source of calcium for anhydrite was carbonates, which decompose under thermal exposure.

The observed surface roughening and formation of technogenic minerals are consistent with recent studies of the thermal alteration of carbonate mineral matrices. However, the widespread formation of needle-shaped crystals composed of Ca, Mg, Si, and O

Fig. 15. SEM images illustrating key structural alterations observed. (**a**) Formation of anhydrite as inclusions consisting of separate elongated, oriented grains (sample 19); (**b**) formation of anhydrite aggregates filling pore spaces (sample 19); (**c**) evidence of dolomite edge destruction (sample 19); (**d**) complete transformation of a dolomite crystal into a nanocrystalline aggregate with needle-like and shapeless drip-like forms (sample 17); (**e**) widespread formation of needle crystal aggregates filling pore spaces (sample 17); (**f**, **g**) formation of needle-like crystals on the surface of dolomite crystals (sample 17). Yellow circles show the location at which samples were analyzed.

Table 5
Results of point analysis of elemental composition (EDX).

Point	Element mass, %					
	Oxygen	Magnesium	Calcium	Sulphur	Carbon	Silicon
1	37.80	4.56	31.71	23.71	2.23	–
2	49.55	10.05	24.84	11.51	4.05	–
3	56.63	13.69	26.88	2.80	–	–
4	51.02	11.89	6.53	–	–	30.57
5	44.29	5.18	37.35	–	1.72	11.47

which we observed to occlude up to 50% of the pore volume, represents a key mechanism for permeability damage that has not been previously incorporated into geochemical models of carbonate alteration during thermal EOR (Askarova et al., 2025).

In this work, we hypothesize that the observed needle-like crystals are magnesium-calcium hydrosilicate (CaH_2MgO_5Si) with a complex crystal structure. The experimental conditions, involving temperatures up to 700 C, are consistent with reported formation temperatures for similar compounds (Karamov et al., 2022; Siauciunas et al., 2021). Additionally, their formation aligns with studies of the thermal treatment of carbonates (Lothenbach et al., 2015).

Further investigation using XRD analysis at higher concentrations is required to conclusively determine the specific mineralogical characteristics of the needle-like crystals. Nonetheless, their formation appears to complicate the pore structure by introducing new crystal growths while simultaneously occupying pore space due to dolomite decomposition.

3.4. Stable isotope analysis of C, H, N, S, and O using isotope ratio mass spectrometry (EA-IRMS)

The molecular and isotopic composition of gases generated during the experiment is presented in Tables 6 and 7. The total hydrocarbon gas content does not exceed 1.5%, with methane comprising 0.62% of the mixture. The molecular composition is dominated by nitrogen (up to 69%) and carbon dioxide (up to 28%), while hydrocarbon homologs from ethane to pentane are minute. This suggests high-temperature cracking of oil, as confirmed by the Bernard diagram (Fig. 16(a)) (Bernard et al., 1978). Furthermore, the co-existence of high concentrations of rock-derived CO_2 with H_2 generated from aquathermolysis could potentially facilitate secondary methanation or Fischer-Tropsch-type reactions, providing an additional pathway for methane formation alongside thermal cracking.

Methane shows $\delta^{13}C$ values ranging from 30.6 to 38.3 (PDB) and $\delta^{2}H$ values from 278 to 299 (VSMOW), indicating isotope fractionation with enrichment in the lighter carbon isotope, ^{12}C. These values are consistent with thermogenic origins (Fig. 16(b)) (He et al., 2019).

The $\delta^{2}H$ values of methane are significantly shifted to more negative “hydrothermal” values compared to gases formed during kerogen cracking. This shift may result from the presence of

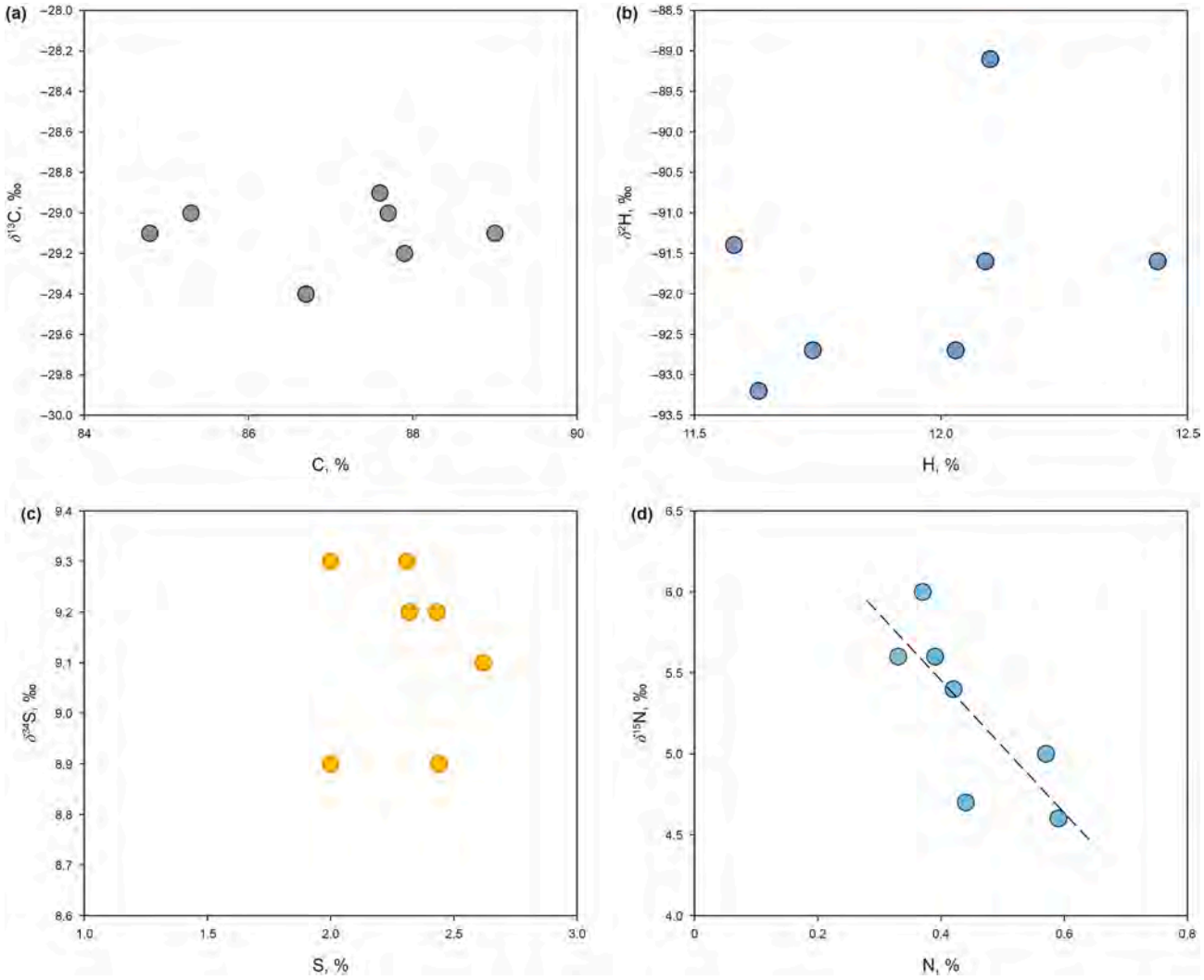

Fig. 18. Dependence of isotope and elemental composition. (**a c**) shows no significant correlations; (**d**) nitrogen isotopic composition becomes heavier with decreasing nitrogen content.

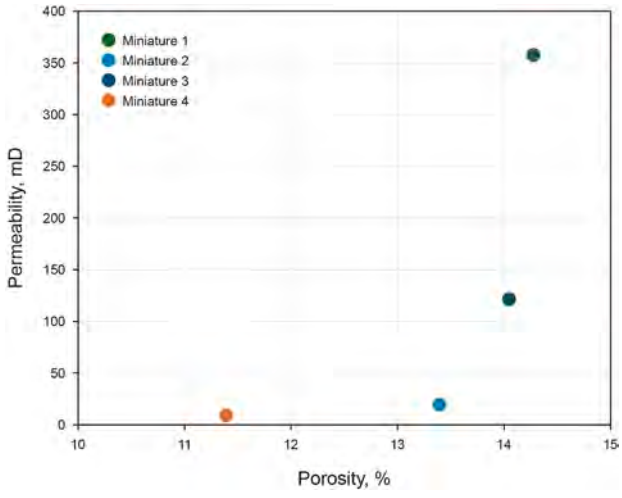

Fig. 19. Original permeability and porosity of miniature core plugs.

mass loss that occurred in the big core plugs was significantly less (around 4%) (Fig. 21). By interpolation (Fig. 21), the actual temperature that the core plugs experienced during the ISC test can be found, which corresponds to about 480–490 C.

The porosimetry measured reservoir rock properties before and after the heating are shown in Fig. 22, where 2 out of 3 samples showed an improvement in the permeability values. The black marks represent the original values, while the red marks are the values after heat exposure.

To increase the statistical sample size and develop an understanding of the permeability change with the dolomite decomposition, an additional five core plugs (Core plugs A–E), sampled from the same outcrop as the big core plugs, were tested. As a drastic mass change was observed at the temperature of 650 C after 4 h of heating, the rest of the samples underwent isothermal heating at 650 C for 4 h as well. Like the previous experiments, the permeability and porosity were measured before and after the core decomposition test, and the results are presented in Fig. 23. The mass loss (before and after the core decomposition tests) varied between 21% and 23% from the initial sample weights. For the consistency of

Fig. 20. Photographs of Whole, Vuggy, and Brine saturated cores.

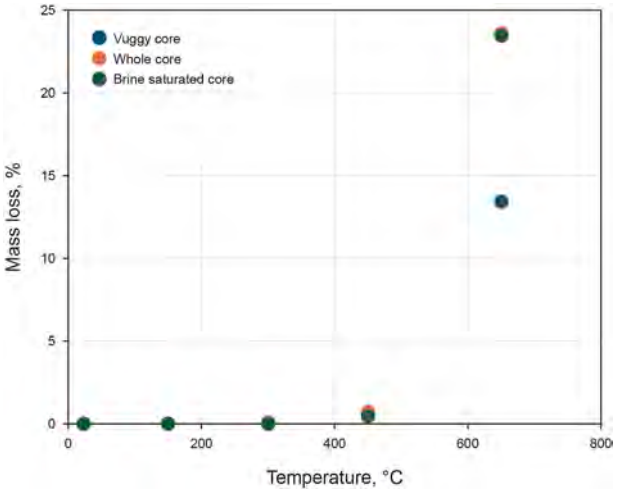

Fig. 21. Mass loss of Whole, Vuggy, and Brine saturated cores.

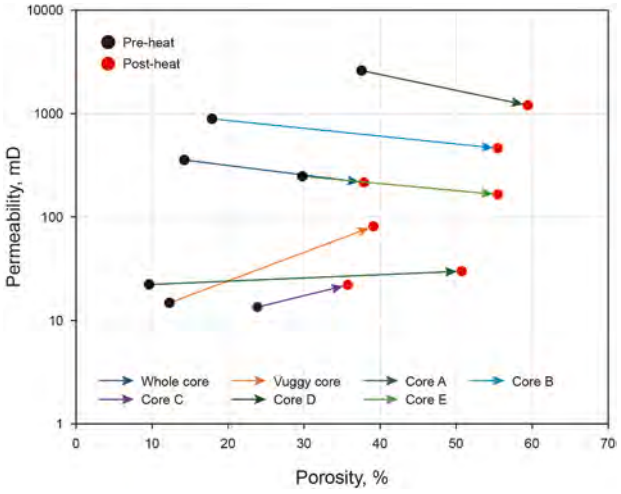

Fig. 23. Permeability and porosity of miniature cores.

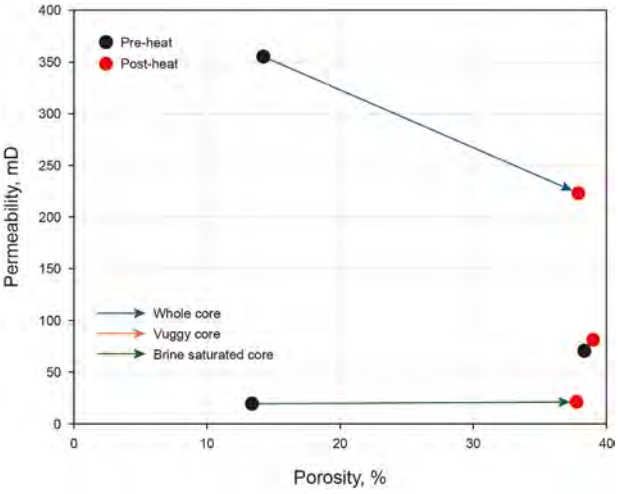

Fig. 22. Permeability and porosity of Whole, Vuggy, and Brine saturated cores.

the compared samples, the Vuggy core plug was excluded from further core evaluation. The black marks represent the original values, while the red marks are the values after heat exposure.

Having analyzed the tendency of the permeability change, it was found that four of the seven samples demonstrated a decrease in permeability. However, this observation was relevant to the samples, in which original permeability varied between 247 and 2600 mD, or in other words for relatively highly permeable samples. To achieve stable permeability values each test was repeated at least 5 times. Every cycle, when helium passed through the core body, the permeability increased (Fig. 24). This approach was fundamental not only to obtain consistency in the measured values but also to imitate a similar case in the field where air injection is a continuous process. Hence, the permeability increase could be justified by the fine migration within the matrix, where the decomposed particles get rearranged with the gas stream.

In the case of the low-permeable (13–247 mD) core plugs, the permeability values improved from between 24% to more than 500% depending on the sample.

To try to understand why certain samples demonstrated an increase in permeability values, while other core plugs deteriorated, the correlation between porosity and permeability was considered in relationship to the rock fabric number (λ), an aspect that likely has not been considered previously in the in-situ combustion literature. Rock fabric, in geological terms, refers to the characterization of the pore space within a rock, considering the impact of particle size and sorting on the interrelationship

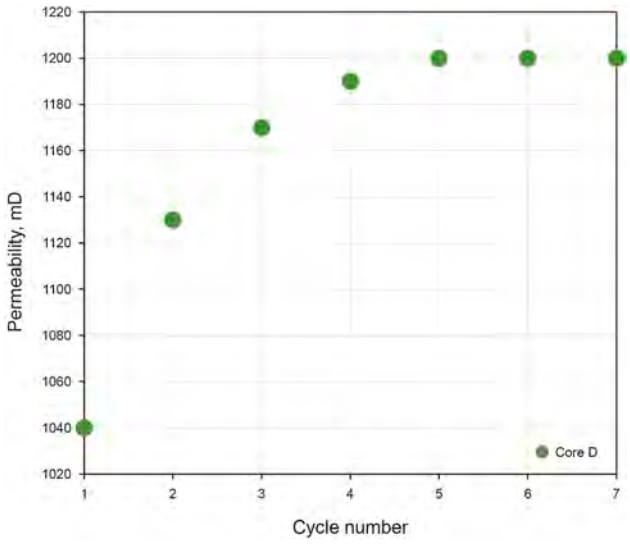

Fig. 24. Permeability measurements of Core D.

between porosity and permeability. When λ ranges between 0.5 and 1.5 the carbonate is generally considered to be a grainstone; when λ ranges between 1.5 and 2.5 the carbonate is generally a packstone; when λ ranges between 2.5 and 4.0 the carbonate is generally a wackstone (Fig. 25). The concept of rock fabric number was developed by Jennings and Lucia (2003).

The paradoxical permeability inversion is explained by a competition between two mechanisms, with the outcome dictated by the initial rock fabric:

(1) Pore-throat pugging in grainstones: In high-permeability grainstones, flow occurs through large, well-connected pores. These open spaces facilitate the extensive growth of neoformed, needle-shaped magnesium-calcium hydrosilicate crystals, as observed in our SEM analysis. These crystals physically obstruct large pore throats, causing a catastrophic reduction in permeability.

(2) Induced microfracturing in packstones/wackstones: In low-permeability, matrix-supported rocks, flow is initially restricted to tortuous micropores. The decomposition of dolomite throughout the matrix causes significant solid mass loss (up to 23%) and vigorous internal CO_2 gas generation. This process induces a network of new microfractures that act as new, high-conductivity flow paths, bypassing the original poor pore system. The net effect is a marked improvement in bulk permeability, as the benefit of new fractures outweighs any plugging of the already inefficient micropores.

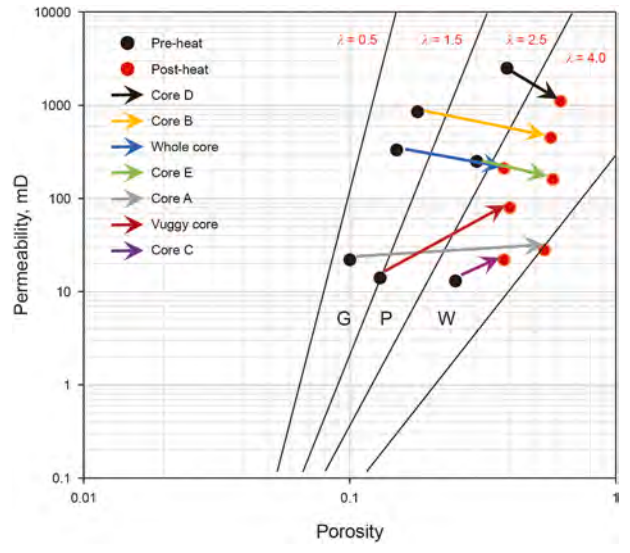

Fig. 25. Rock-fabric number, permeability, and porosity of the core plugs; λ between 0.5 and 1.5 corresponds to grainstone (G) carbonate; λ between 1.5 and 2.5 corresponds to packstone (P), and λ between 2.5 and 4.0 corresponds to wackstone (W). Rock fabric lines after Jennings and Lucia (2003).

While previous experimental studies of thermal EOR in carbonates have reported permeability alterations (Mogensen and Masalmeh, 2020; Mohammadi and Mahmoudi Alemi, 2023; Mukhametdinova et al., 2023), the results have often appeared contradictory, with both damage and stimulation being observed. Our hypothesis is that these conflicting observations can be reconciled by considering the initial rock fabric, an aspect largely overlooked in prior ISC literature. By classifying our samples into grainstones, packstones, and wackstones, we can systematically analyze how the same thermal process leads to divergent permeability responses. This approach moves beyond a simple porosity–permeability relationship and provides a more robust framework for predicting reservoir quality evolution, a critical need for improving the reliability of numerical reservoir simulations (Askarova et al., 2025; Meng et al., 2023).

Another point of interest has to do with the change in pore throat (port) size between pre- and post-heat conditions. The port subject has been summarized by Hartmann and Beaumont (1999) in the AAPG literature and has been demonstrated with different types of rocks including carbonates by Aguilera (2014).

Hartmann and Beaumont (1999) indicate that analyzing permeability and porosity data separately to characterize rock quality can be deceiving. It is more effective to work with the ratio of permeability and porosity for determining rock quality or to go beyond it for estimating the pore throat aperture of the rocks. This is done in Fig. 26, where r_{p35} is the radius of the pore throat aperture at 35% cumulative pore volume. This type of graph is generally referred to as a flow units plot.

Dale Winland, an Amoco researcher, found that the effective pore system that dominates flow through a rock generally corresponds to a mercury saturation of 35% during a capillary pressure test (Winland, 1972). Fig. 25 includes the same pre- and post-heat porosities and permeabilities presented in Figs. 22 and 24. The crossplot shows megaports (r_{p35} > 10 μm), macroports (2 to 10 μm), mesoports (0.5 to 2 μm), and microports (0.1 to 0.5 μm).

The three upper samples (black dots) fall within the megaport region with large pore throat radii. at original preheating conditions. Following in-situ combustion the samples (red dots) show significant reductions in permeability and pore throat aperture. Samples with pre-heat permeabilities below 100 mD show some post-heat increase; however, their pore throat radii remain approximately the same in the lower part of the macroport region.

The conclusion is reached that the reduction in post-heat port throat radii illustrated by the red dots is consistent with the rock fabric number discussed above which shows a reduction in the quality of the rocks. These findings might prove of value in future combustion tests and reservoir simulation studies.

Flow unit description shown in Fig. 26 shows that three pre-heat cores (black dots) fall in the region dominated by megaports, one sample in the upper macroport region and three samples in the lower macroport region. Thus, all the samples have

Fig. 26. Pore throat radii, permeability, and porosity for the pre- and post-heat core plugs, r_{p35} lines after Aguilera (2014).

important radii at original conditions. Following in-situ combustion the samples (red dots) show important reductions in permeability. Samples with pre-heat permeabilities below 100 mD show some post-heat increase; however, their pore throat radii remain approximately the same in the lower part of the macroport region.

It should be noted that the experiments described above differ from actual in-situ ISC conditions as they were done at atmospheric pressure, without oil or brine saturation, and did not undergo a combustion process. Hence, it is recommended to evaluate these experiments keeping into account all the nuances to evaluate the adequacy of the obtained findings.

4. Conclusions

This multi-scale, post-combustion analysis of a vuggy dolomite reservoir reveals that in-situ combustion (ISC) induces a fundamental and paradoxical permeability inversion. The primary quantitative finding is that initially high-permeability samples (up to 2600 mD) experienced significant permeability damage, while initially low-permeability samples (<250 mD) showed marked improvement. This was accompanied by a significant reduction in pore throat radii, with the flow regime shifting from a megaport-dominated to a macroport-dominated system.

The mechanism driving this inversion is the thermal decomposition of the rock matrix at temperatures of 480–490 C, leading to a significant mass loss of the rock (up to 23%). This process fundamentally altered the rock fabric, transforming it from a high-quality grainstone/packstone (rock-fabric number, λ 1.5–2.5) to a low-quality wackstone-like character (λ 4.0).

Micro-scale analysis provided direct evidence for this mechanism. The neoformation of pore-occluding, needle-shaped magnesium-calcium hydrosilicate crystals was observed, occupying up to 50% of the pore space in high-quality rock. The dominance of this mineralogical reaction over oil burning was confirmed by stable isotope analysis, which quantified that up to 70% of the produced CO_2 originated from dolomite decomposition, with only 30% derived from hydrocarbon combustion.

The implications of these findings are critical for the planning and monitoring of ISC projects in carbonate reservoirs. First, initial permeability and porosity alone are poor predictors of post-combustion reservoir quality; the geochemical reactivity and thermal stability of the rock fabric are paramount. The rock-fabric number (λ) may serve as a more robust metric for predicting a reservoir's response to thermal stress. Second, produced gas analysis must account for the significant contribution of mineral-derived CO_2 to accurately assess combustion front efficiency and stoichiometry.

Ultimately, this work provides a rock-based, mechanistic framework for understanding reservoir alteration during ISC, but further research is needed. Future experimental work should investigate the impact of confining pressure and brine chemistry on these mineralogical transformations. A critical parallel challenge is the upscaling of these core-scale findings for reservoir simulation. Predictive models must evolve to incorporate rock-fabric-dependent alterations, including dynamic changes in relative permeability, geomechanical properties, and potentially transitioning to dual-porosity frameworks to account for induced microfracturing. Integrating these complex mechanisms is paramount for refining predictive models and accurately forecasting ISC performance in heterogeneous carbonate systems.

CRediT authorship contribution statement

Rita Fazlyeva: Writing – review & editing, Writing – original draft, Visualization, Investigation, Formal analysis, Data curation, Conceptualization. **Tagir Karamov:** Writing – review & editing, Writing – original draft, Visualization, Methodology, Investigation. **Matthew Ursenbach:** Supervision, Methodology, Conceptualization. **Roberto Aguilera:** Validation, Resources, Project administration, Formal analysis. **Andrey Voropaev:** Methodology, Investigation. **Mikhail Spasennykh:** Writing – review & editing, Supervision, Resources, Project administration, Funding acquisition, Formal analysis. **Gordon Moore:** Writing – review & editing, Supervision, Resources. **Alexey Cheremisin:** Resources, Project administration. **Mehta Sudarshan:** Writing – review & editing, Supervision, Project administration, Methodology, Investigation, Conceptualization.

Declaration of competing interest

The authors declare that they have no known competing financial interests or personal relationships that could have appeared to influence the work reported in this paper.

References

Aguilera, R., 2014. Flow units: From conventional to tight gas to shale gas to tight oil to shale oil reservoirs. In: SPE Reservoir Eval. Eng. https://doi.org/10.2118/165360-PA.

Akbar, M., Vissapragada, B., Alghamdi, A.H., Allen, D., Herron, M., Carnegie, A., Dutta, D., Olesen, J.-R., Chourasiya, R.D., Logan, D., Stief, D., Netherwood, R., Russell, S.D., Saxena, K., 2000. A snapshot of carbonate reservoir evaluation. Oilfield Rev. 12, 20–41.

Alizadeh, A., 2020. A Robust Kinetic Model for Computer Modelling of In Situ Combustion Processes in Athabasca Oil Sands. Doctoral Dissertation. University of Calgary, Alberta, Canada.

Antolinez, J.D., Miri, R., Nouri, A., 2023. In situ combustion: A comprehensive review of the current state of knowledge. Energies 16 (17). https://doi.org/10.3390/en16176306.

Askarova, A., Alekhina, T., Fazlyeva, R., Popov, E., Mehta, S.R., Moore, R.G., Ursenbach, M.G., Cheremisin, A., 2025. In situ combustion performance in heavy